Surface reconstructions of LaCo$_{1-x}$Fe$_x$O$_3$ at high temperature during N$_2$O decomposition in realistic exhaust gas composition: Impact on the catalytic properties

CrossMark

Y. Wu[a], C. Cordier[b], E. Berrier[a], N. Nuns[a], C. Dujardin[a], P. Granger[a],*

[a] Unité de Catalyse et de Chimie du Solide, UMR 8181, Université Lille1 Sciences et Technologies, Cité Scientifique, bâtiment C3 59655, Villeneuve d'Ascq, France
[b] Unité Matériaux Et Transformations, UMR 8207, Université Lille1 Sciences et Technologies, Cité Scientifique, bâtiment C6, 59655, Villeneuve d'Ascq, France

ARTICLE INFO

ABSTRACT

This study is dedicated to the development of thermally stable LaCo$_{1-x}$Fe$_x$O$_3$ perovskite based catalysts for the decomposition of N$_2$O at medium and high temperature, in representative compositions of exhaust gas from ammonia burner in nitric acid plants. In these specific conditions, N$_2$O coexists with a large amount of NO$_x$. Up to now, lab-scale investigations were usually restricted to low amount of NO$_x$ and water while both can originate drastic changes in the catalytic performances related to activation/deactivation phenomena. The impact of NO concentration in terms of activity and stability has been discussed at moderate temperature and correlated to extensive bulk and surface characterization from different techniques (X-ray diffraction, Raman spectroscopy, XPS, Mössbauer spectroscopy, Tof-SIMS). It was found that the catalytic performances in terms of activity and stability depend on the relative concentration of Co with the best performances recorded on LaCo$_{0.2}$Fe$_{0.8}$O$_3$.

1. Introduction

Catalytic abatement of N$_2$O emissions coming from stationary sources represents an outstanding issue because N$_2$O exhibits a much higher global warming potential than CO$_2$ and a longer lifetime. Previous investigations were essentially focused on exhaust gas from adipic acid plants containing high concentration of N$_2$O (30–50 vol.%) as side product [1,2]. In this specific application, lab-scale optimization was achieved at medium temperature in the absence of significant amount of water in the exhaust gas [3]. Regarding nitric acid plants, N$_2$O is produced in substantially lower amount on aged Pt-Rh gauzes in the ammonia burner which implies the development of intrinsically more active catalysts. Previous investigations revealed the feasibility of catalytic abatement processes running at high temperature inside the ammonia burner instead of end-of-pipe technologies for which the use of reducing agents is usually a pre-requisite step [4]. However, the installation of catalytic abatement processes to decompose N$_2$O in the ammonia burner with residual temperature up to 900 °C is a challenging task since the low thermal stability of catalysts might represent a serious obstacle for further practical developments

[2,3]. Hence, the lifetime and the selectivity of the catalyst must be improved especially to avoid simultaneous conversion of NO and related loss of nitric acid yield. Bulk or supported mixed metal oxides and metal-loaded zeolites were previously developed for catalytic N$_2$O decomposition in nitric acid plants, e.g. Co$_2$AlO$_4$/CeO$_2$ by Yara International, CuO/Al$_2$O$_3$ by BASF and Fe/ZSM-5 by Uhde [5]. Alternative catalytic formulations were evaluated at the lab-scale for N$_2$O decomposition, such as yttrium stabilized zirconia [6], Fe–Ce mixed oxides [7], ceria-zirconia [8], Fe$_2$O$_3$/Al$_2$O$_3$ [9] and metal-substituted hexaaluminates [10]. Only few examples of perovskite-based catalysts are described in the patents. By way of illustration, Porzellanwerk Kloster Veilsdor proposed supported LaCoO$_3$ perovskite as active component for N$_2$O decomposition at high temperature [11]. Umicore also patented various formulations of perovskites for the decomposition of N$_2$O [12].

Recently, Kondratenko et al. reported outstanding kinetic information from TAP measurements under ultra-high-vacuum (UHV) by comparing kinetic parameters on BaFeAl$_{11}$O$_{19}$ and Fe-MFI zeolites highlighting the importance of the degree of isolation of the active phase (isolated versus oligomeric iron species) on the estimates of kinetic parameters [13,14]. However, one have to mention that most of those studies report catalytic data sometimes far from the real exhaust gas conditions since representative operating conditions should take ~10 vol% H$_2$O and significant higher amount of NO into account. Perovskite-based materials (ABO$_3$)

* Corresponding author. Tel.: +33 320 434 938; fax: +33 320 436 561.
E-mail address: pascal.granger@univ-lille1.fr (P. Granger).

might be attractive for catalytic application due to their low cost of production. Moreover, perovskites can serve as a host structure. Non-stoichiometry and partial substitution of A and B cations within the structure tolerance can bring about different electronic properties [15]. Hence, it is possible to tune the bulk and surface properties of perovskite by incorporation of appropriate promoters according to the selected applications. Our previous investigations showed the potential interest of $LaCoO_3$ in the catalytic decomposition of N_2O from nitric acid plants [16]. It was suggested that oxygen mobility governs the catalytic properties with in situ formation of anionic vacancies at high temperature which can be potentially active for further adsorption and decomposition of N_2O. However, surface reconstructions activated at high temperature can induce significant alterations of the bulk and surface mobility of oxygen which make further decisive conclusions on the real composition of active sites uncertain.

In the present work, we have investigated the influence of iron incorporation to $LaCoO_3$ on the thermal stability and related catalytic performances in the decomposition of N_2O under realistic mixture. Particular attention was also paid to the impact of NO concentration. In the presence of high amount of NO, representative of the NO_x concentration in ammonia burner, drastic changes in the catalytic performances were observed which diverge from those obtained at much lower NO concentration. Such apparent controversy has been tentatively explained on the basis of extensive bulk and surface characterization.

2. Experimental

2.1. Catalyst preparation and characterization

Perovskite-based catalysts $LaCo_{1-x}Fe_xO_3$ ($x = 0$, 0.2, 0.4, 0.6, 0.8, 1) were synthesized according to a conventional sol–gel method involving a citrate route [17] using aqueous solutions of $La(NO_3)_3 \cdot 6H_2O$, $Co(NO_3)_2 \cdot 6H_2O$ and $Fe(NO_3)_3 \cdot 9H_2O$ with a molar citric acid/(La + Co + Fe) ratio of 1. The solid was obtained after evaporation, drying overnight at 90 °C and calcination in air at 900 °C for 8 h. Specific surface area was calculated from nitrogen physisorption measurements at −196 °C by using a FlowSorb III apparatus.

Powder X-ray diffraction (XRD) was performed at room temperature using a Bruker AXS D8 Advance diffractometer working in Bragg-Brentano geometry and equipped with a LynxEye Super Speed detector. Data were collected with Cu Kα ($\lambda = 0.154$ nm) in the 10–100° 2θ range with a 0.02° 2θ step. The Fullprof Suite program [18,19] was used for Rietveld refinement. The Thompson-Cox-Hastings pseudo-Voigt function was chosen for peak profiles. LaB_6 was used as standard to derive the instrument resolution. An isotropic size parameter of Gaussian character was refined to take the contribution of sample in the broadening of Bragg peaks into account. Raman spectra were recorded on a Labram HR Jobin Yvon spectrometer using a frequency-doubled Nd:YAG laser corresponding to an excitation wavelength of 532 nm. A 100× microscope objective was used to focus the excitation beam and collect the scattered light through a confocal hole (100 μm) further analyzed by a high resolution spectrometer. The silicon line at 520 cm^{-1} was used for calibration before each measurement. Tof-SIMS analysis was carried out using a Tof-SIMS V instrument (ION-TOF GmbH Germany) equipped with a Bi liquid metal ion gun (LMIG). Pulsed Bi^{3+} primary ions were used for analysis (25 KV, 0.25 pA). Three surface spectra were taken for each sample over an area of 500 μm × 500 μm during 100 s. These experimental conditions allowed staying within the static SIMS since primary ion dose did not exceed 10^{12} ions/cm^2. Charging effects, due to the primary ion beam, were compensated by using pulsed low energy electrons (20 eV). XPS experiments were performed on an AXIS

Ultra DLD Kratos spectrometer equipped with a monochromatized aluminium source for excitation (150 W) and charge compensation. The analyzer was operated in a constant pass energy mode ($E_{pass} = 40$ eV). All binding energies were referenced to the C 1s core level at 285 eV. Peak area was estimated after subtracting the background according to the procedure suggested by Shirley [20]. Special attention was paid to the quantification of surface Co and Fe concentrations taking into account the Auger contributions from Fe and Co respectively. *Ex situ* Mössbauer spectra were recorded at room temperature using a ^{57}Co (Rh) source. Constant acceleration mode and transmission geometry were used during acquisition. Data fitting was performed with Lorentzian shape peaks and hyperfine parameters (hyperfine field (HF), isomer shift (IS), quadrupole splitting (QS)) were calculated with metallic iron as reference.

2.2. Catalytic activity measurements

Catalytic decomposition of N_2O was studied in a fixed-bed flow reactor using 0.7 g of catalyst with a total flow rate of 15 L h^{-1} within a temperature range 100–900 °C. The reaction mixture was composed of 0.1 vol% N_2O, 0.5 or 5 vol% NO, 6 vol% O_2, 15 vol% H_2O and He balance. A first temperature-programmed reaction experiment (heating rate 2 °C/min) was systematically carried out on all calcined samples which were ultimately maintained overnight at 900 °C under reaction mixture. After cooling down to 100 °C, a second temperature-programmed reaction experiment was performed on aged samples in similar conditions in order to evaluate the impact of thermal ageing at 900 °C on the catalytic performances. The outlet effluents were quantified with a NO_x analyzer (Thermo 42i-HL) using chemiluminescence detector for NO and NO_2 and a dispersive IR analyzer for N_2O detection (Emerson XStream).

3. Results

3.1. Catalytic performances in the decomposition of N_2O

A first series of catalytic measurements was performed according to the procedure described in the experimental section. The simulated mixture was composed of 0.1 vol% N_2O, 6 vol% O_2 and 15 vol% H_2O with low amount of 0.5 vol% NO. A second series was performed in more realistic conditions with one order of magnitude higher NO concentration.

3.1.1. In the presence of 0.5 vol% NO

As shown in Fig. 1, temperature-programmed experiments on calcined $LaCo_{1-x}Fe_xO_3$ reveal the occurrence of two major reactions. Below 600 °C, a typical volcano-type curve is observable (see Fig. 1A) characteristic of the oxidation of NO to NO_2 then becoming thermodynamically limited with a raise in temperature. Obviously, the extent of such reaction depends on the catalyst composition showing a rate enhancement in NO_2 production after Fe incorporation to $LaCoO_3$. The oxidation of NO to NO_2 has been previously studied on perovskite based materials [21] with similar trends after Ce incorporation to $LaCoO_3$ compared with those observed in this study. The authors suggested that adsorbed oxygen species on the surface might play an important role in the reaction with subsequent stabilization of strongly chemisorbed ad-NO_x species.

At $T > 450$ °C, Fig. 1B shows temperature-programmed experiments for the catalytic decomposition of N_2O to N_2 on calcined samples. The nitrogen balance established at high temperature ($T > 800$ °C) confirms an exclusive selectivity towards N_2O decomposition on $LaCo_{1-x}Fe_xO_3$ with no NO loss. N_2O conversion curves clearly show the poorest catalytic performances of $LaFeO_3$. The following activity sequence can be qualitatively established based on the estimation of the light-off temperature
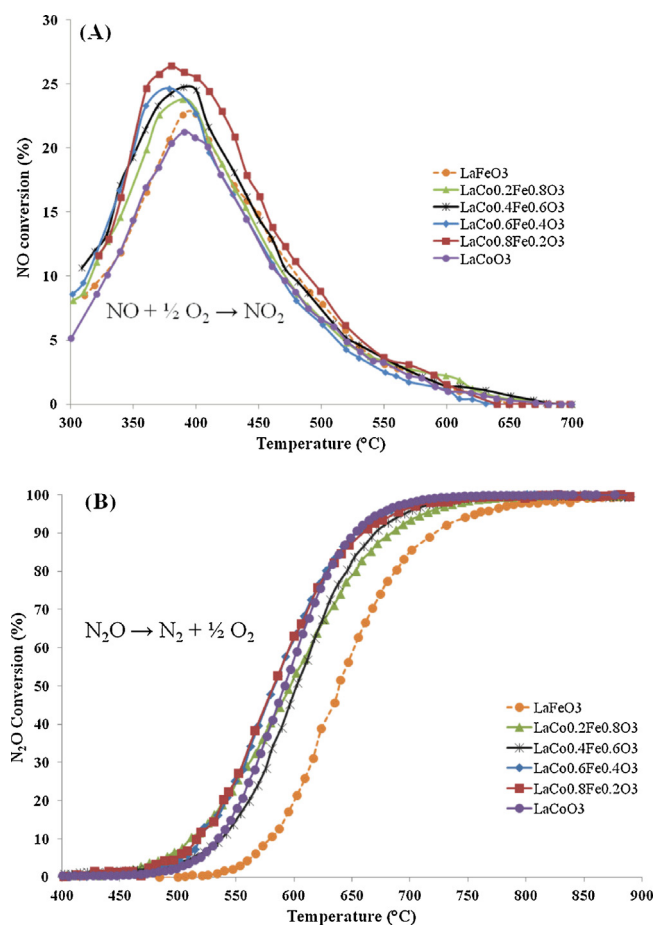
Fig. 1. NO conversion profile to NO_2 (A); N_2O decomposition profile to N_2 during temperature-programmed experiments with 0.5 vol% NO on calcined $LaCo_{1-x}Fe_xO_3$ catalysts.

Fig. 2. Arrhenius plots ln k vs. $1/T$ for the decomposition of N_2O restricted to conversion in the range 5–15% during the temperature-programmed reaction with 0.1 vol% N_2O, 0.5 vol% NO, 6 vol% O_2 and 15 vol% H_2O on calcined (A) and aged (B) $LaCo_{1-x}Fe_xO_3$ catalysts.

(T_{50}) corresponding to 50% N_2O conversion reported in Table 1: $LaFeO_3 < LaCo_{0.4}Fe_{0.6}O_3 < LaCo_{0.2}Fe_{0.8}O_3 < LaCoO_3 < LaCo_{0.8}Fe_{0.2}O_3 = LaCo_{0.6}Fe_{0.4}O_3$. This sequence clearly indicates that the activity below the light-off temperature is related to the presence of cobalt. However, the incorporation of iron enhances the conversion on $LaCo_{0.8}Fe_{0.2}O_3$ and $LaCo_{0.6}Fe_{0.4}O_3$. Such a trend still remains on aged samples exposed overnight at 900 °C under reaction mixture. It is worthwhile to mention that the extent of deactivation cannot be simply explained by a loss of specific surface area (SSA). On calcined samples, SSA remains quasi-unchanged according to the margin of error varying in the range 4.4–5.6 $m^2\,g^{-1}$. Specific surface area on aged samples slightly decreases to $\sim 3\,m^2\,g^{-1}$ with negligible variations irrespective of the iron content.

Apparent activation energy values (E_{app}), reported in Table 1, have been estimated from the slope of the Arrhenius plots ln k vs. $1/T$ reported in Fig. 2. The rate constant values k have been calculated from Eq. (1) where X_{N_2O} stands for the conversion of N_2O, W the mass of catalyst and Q_0 the total flow rate. Eq. (1) is valid for a plug flow reactor and takes a first order kinetic reaction for N_2O decomposition into account [1]. This latter assumption has been verified in this present study on $LaCoO_3$ from steady state kinetic measurements (results not shown). The calculations of E_{app} on calcined and aged samples take N_2O conversion X_{N_2O} in the range 5–15% into account corresponding to a low temperature range 475–600 °C. It was also verified that the estimates of kinetic parameters was not altered due to thermal decomposition of N_2O.

Table 1
Catalytic performances in N_2O decomposition in the presence of 0.5 vol% NO.

	T_{50}[a] (°C)		ΔT_{50} (°C)	Activation energy E_{app} (kJ/mol)		Pre-exponential factor (L h^{-1} g^{-1})		Specific rate[b] ($\times 10^{-5}$ mol h^{-1} g^{-1})		Intrinsic rate[c] ($\times 10^{-2}$ mol h^{-1} surf Co at^{-1})	
	Calcined	Aged		Calcined	Aged	Calcined	Aged	Calcined	Aged	Calcined	Aged
$LaCoO_3$	592	613	21	222	178	5.2×10^{14}	4.6×10^{11}	6.7	4.8	2.8	2.2
$LaCo_{0.8}Fe_{0.2}O_3$	582	603	21	187	169	4.8×10^{12}	2.7×10^{11}	12.4	10.0	5.6	5.3
$LaCo_{0.6}Fe_{0.4}O_3$	582	617	35	211	172	1.8×10^{14}	2.2×10^{11}	13.4	5.3	6.6	3.4
$LaCo_{0.4}Fe_{0.6}O_3$	602	632	30	164	173	8.6×10^{10}	1.5×10^{11}	6.7	2.9	5.7	2.4
$LaCo_{0.2}Fe_{0.8}O_3$	597	628	31	144	149	8.7×10^{9}	9.6×10^{9}	13.4	7.2	21.8	14.7
$LaFeO_3$	638	673	35	237	200	7.5×10^{14}	2.0×10^{12}	0.5	–	–	–

[a] T_{50}: Temperature corresponding to 50% conversion of N_2O.
[b] Specific reaction rate at 525 °C was normalized by mass of catalyst.
[c] Intrinsic reaction rate at 525 °C was normalized by cobalt atom accessible on the surface according to XPS analysis.
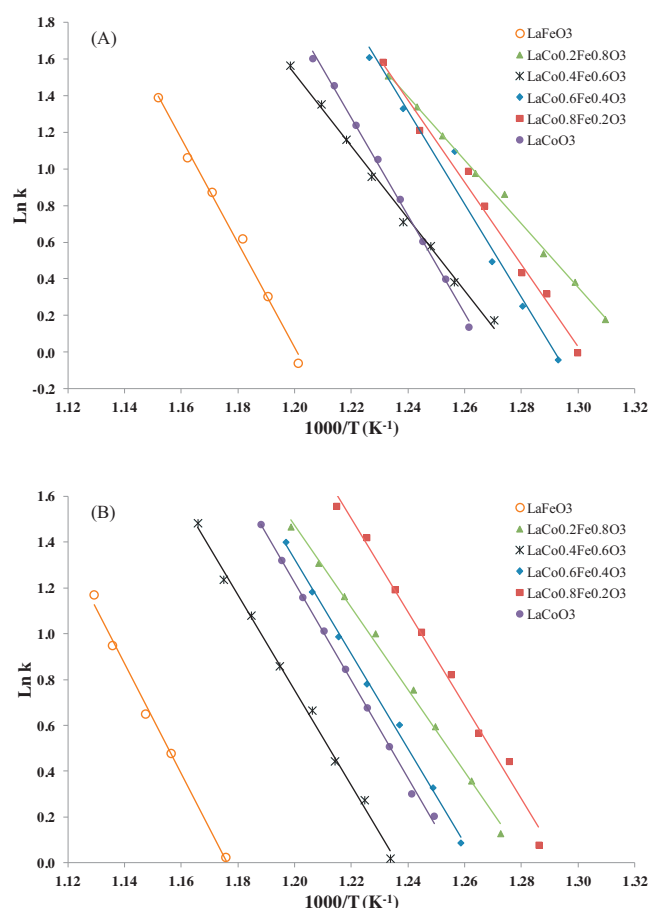
Table 2
Catalytic performances in N_2O decomposition in the presence of 5 vol% NO.

	T_{50}[a] (°C)		ΔT_{50} (°C)	Activation energy E_{app} (kJ/mol)		Pre-exponential factor (L h^{-1} g^{-1})		Specific rate[b] ($\times 10^{-5}$ mol h^{-1} g^{-1})		Intrinsic rate[c] ($\times 10^{-2}$ mol h^{-1} surf Co at^{-1})	
	Calcined	Aged		Calcined	Aged	Calcined	Aged	Calcined	Aged	Calcined	Aged
LaCoO$_3$	580	641	61	209	172	8.3×10^{13}	8.3×10^{10}	7.4	2.6	3.1	1.2
LaCo$_{0.8}$Fe$_{0.2}$O$_3$	564	648	84	200	162	3.9×10^{13}	2.4×10^{10}	12.9	2.9	5.9	1.4
LaCo$_{0.6}$Fe$_{0.4}$O$_3$	588	635	47	201	148	3.4×10^{13}	4.6×10^{9}	10.0	4.2	4.9	2.9
LaCo$_{0.4}$Fe$_{0.6}$O$_3$	616	650	34	167	155	1.2×10^{11}	7.7×10^{9}	6.5	3.2	5.6	2.7
LaCo$_{0.2}$Fe$_{0.8}$O$_3$	626	666	40	148	141	6.5×10^{9}	1.3×10^{9}	6.2	3.4	10.1	8.9
LaFeO$_3$	680	707	27	196	179	8.7×10^{11}	5.3×10^{10}	–	–	–	–

[a] T_{50}: Temperature corresponding to 50% conversion of N_2O.
[b] Specific reaction rate at 525 °C was normalized by mass of catalyst.
[c] Intrinsic reaction rate at 525 °C was normalized by cobalt atom accessible on the surface according to XPS analysis.

In addition, preliminary experiments and calculations confirmed the absence of external and internal diffusion limitations in this conversion and temperature range which emphasizes the fact that these measurements were performed in chemical regime as earlier checked on the same variety of catalysts [22].

$$k = \frac{Q_0}{W} \ln \left(\frac{1}{1 - X_{N_2O}} \right) \qquad (1)$$

Further comparisons in Table 1 show numerical solutions for E_{app} values of the same order of magnitude as those earlier reported [1]. The highest value calculated on LaFeO$_3$ can explain its lowest specific activity almost nil demonstrating the involvement of cobalt as active sites in the catalytic decomposition of N_2O at moderate temperature ($T \leq 600$ °C). Obviously, the introduction of iron in the perovskite structure drastically decreases the apparent activation energy especially on LaCo$_{0.2}$Fe$_{0.8}$O$_3$ which correctly explains the unexpected high intrinsic rate expressed per surface Co atom. However, a compensating effect is observed related to a sharp drop of the pre-exponential factor probably related to a significant lowering in the density of cobalt active sites for Fe-riched samples. This effect is noticeable on LaCo$_{0.2}$Fe$_{0.8}$O$_3$ which largely contributes to lessen its specific activity. It is worthwhile to note that LaCo$_{1-x}$Fe$_x$O$_3$ behave differently towards deactivation depending on the iron composition x. For Co-riched samples ($x \leq 0.4$), thermal ageing overnight at 900 °C leads to a significant decrease of the apparent activation energy while numerical solutions provided for Fe-riched samples slightly vary likely within the margin of error. Regarding the pre-exponential factor, the same trends are noticeable with a compensating effect due to a sharp drop in the estimated values for $x \leq 0.4$. On the other hand, the numerical values remain quasi-unchanged compared to those calculated on calcined samples for $x > 0.4$.

3.1.2. In the presence of 5 vol% NO

The same methodology was implemented for characterizing the impact of higher NO concentration on the adsorptive properties of calcined and aged LaCo$_{1-x}$Fe$_x$O$_3$ samples in the decomposition of N_2O. Similarly, no detectable NO conversion was found at high temperature above 800 °C which makes the prepared perovskite-based catalysts LaCo$_{1-x}$Fe$_x$O$_3$ suitable for the selected application in this study. Fig. S1 illustrates different impacts of NO concentration on the catalytic properties of calcined LaCoO$_3$ (A) and LaFeO$_3$ (B). It seems obvious that NO inhibits the conversion of N_2O at low temperature on LaCoO$_3$. This behavior seems in correct agreement with previous observations relating this effect to a significant production of NO$_2$ in this temperature range with subsequent stabilization of strongly chemisorbed nitrate species [16]. On the other hand, the rate of N_2O conversion taking place on LaCoO$_3$ at higher temperature is insensitive to change in NO concentration from 0.5 to 5 vol% except above the light-off temperature since a slight improvement is discernible. On the contrary, it is obvious that high

NO concentration strongly inhibits N_2O conversion on LaFeO$_3$. Fig. S2 illustrates temperature-programmed N_2O conversion curves recorded on calcined and aged LaCo$_{1-x}$Fe$_x$O$_3$. Clearly the same tendency earlier depicted in the presence of 0.5 vol% NO persists with better catalytic performances on Co-riched catalysts according to the following reactivity sequence established as previously from the estimated light-off temperatures collected in Table 2: LaCo$_{0.8}$Fe$_{0.2}$O$_3$ > LaCoO$_3$ > LaCo$_{0.6}$Fe$_{0.4}$O$_3$ > LaCo$_{0.4}$Fe$_{0.6}$O$_3$ > LaCo$_{0.2}$Fe$_{0.8}$O$_3$ > LaFeO$_3$. The specific rates calculated at lower temperature ($T = 525$ °C) and conversion when mass transfer phenomena should not occur significantly are still in agreement with the above-mentioned sequence underlining the exaltation of Co catalytic properties after iron incorporation (see intrinsic rates in Table 2). However, it seems obvious that the presence of higher NO concentration strongly enhances deactivation phenomena according to the deviation observed on the light-off temperature, ΔT_{50}. In order to get more obvious comparisons, pre-exponential factors and activation energies were calculated from the Arrhenius plots collected in Fig. 3 from Temperature-programmed conversions on calcined and aged catalysts (see Fig. S2). As a general trend, results reported in Table 2 reveal the same order of magnitude for activation energies on calcined samples in comparison with those previously obtained in the presence of 0.5 vol% NO. However, further comparisons also show slightly lower values on aged catalysts. It is still noticeable that Fe incorporation induces lower apparent activation energies especially on LaCo$_{0.2}$Fe$_{0.8}$O$_3$ as previously found with 0.5 vol% NO. Similarly the compensating effect earlier described is still observed with a significant decrease of the pre-exponential factor related to an increase in the iron content. Further comparisons on aged samples in the presence of 5 vol% NO also indicate that the numerical values are substantially lower than those calculated in the presence of 0.5 vol% NO.

Now, the predicted intrinsic rates at 525 °C reveal comparable kinetic features than those discussed in the previous paragraph with the highest catalytic activity on LaCo$_{0.2}$Fe$_{0.8}$O$_3$ and a loss of activity after ageing. However, it seems obvious that the presence of higher amount of NO in the feed has a detrimental effect with numerical values lower than those previously compared in Table 1.

3.2. Bulk and surface characterization of freshly-prepared LaCo$_{1-x}$Fe$_x$O$_3$

3.2.1. X-ray diffraction measurements

Fig. 4 shows XRD patterns of LaCo$_{1-x}$Fe$_x$O$_3$ samples calcined at 900 °C. They are dominated by the characteristic X-ray lines ascribed to the perovskite phase with no detectable bulk cobalt and iron oxides. Slight segregation of monoclinic La$_2$O$_3$ is found on LaFeO$_3$ at $2\theta \approx 31°$. A transition from rhombohedral to orthorhombic structure is clearly evidenced for $x > 0.5$ in good agreement with previous findings [23]. The substitution of cobalt by iron induces a continuous shift of the X-ray lines towards lower 2θ angles.

Table 3
Structural and textural properties of $LaCo_{1-x}Fe_xO_3$ solids calcined at 900 °C.

	Structure[a]	a (Å)	b (Å)	c (Å)	α (°)	B—O bond length (Å)[b]	Crystallite size (nm)	SSA (m²/g)
$LaCoO_3$	Rhom.	5.380	–	–	60.77	2.690	75	4.6
$LaCo_{0.8}Fe_{0.2}O_3$	Rhom.	5.393	–	–	60.74	2.697	67	4.5
$LaCo_{0.6}Fe_{0.4}O_3$	Rhom.	5.419	–	–	60.70	2.709	53	5.4
$LaCo_{0.4}Fe_{0.6}O_3$	Ortho.	5.466	5.493	7.768	90	2.733	31	5.6
$LaCo_{0.2}Fe_{0.8}O_3$	Ortho.	5.503	5.531	7.806	90	2.752	48	4.6
$LaFeO_3$	Ortho.	5.557	5.558	7.855	90	2.779	34	4.4

[a] Rhom.: Rhombohedral perovskite phase $a = b = c$, $\alpha = \beta = \gamma$; Ortho.: Orthorhombic perovskite phase $a \neq b \neq c$, $\alpha = \beta = \gamma = 90°$.
[b] B—O bond length was supposed to be equal to half of the cell parameter a based on their crystal structure.

Further Rietveld refinement summarized in Table 3, shows a linear increase of the cell parameter a from 5.380 Å for $LaCoO_3$ to 5.557 Å for $LaFeO_3$. Indeed, Fe^{3+} cation has a relatively larger ionic radii of 0.645 Å compared to Co^{3+} of 0.61 Å [24]. Therefore, the substitution of cobalt by iron in the B-site of perovskites would provoke the expansion of the unit cell. To summarize, XRD analysis confirms a preferential formation of bulk solid solutions rather than the segregation of the individual metal oxides for calcined $LaCo_{1-x}Fe_xO_3$ samples. The average crystallite size was also estimated by Rietveld refinement. Among calcined $LaCo_{1-x}Fe_xO_3$ solids, $LaCoO_3$ has the largest crystallite size of approximate 75 nm nearly two times larger than $LaCo_{0.4}Fe_{0.6}O_3$ and $LaFeO_3$ (see Table 3).

3.2.2. Raman spectroscopic measurements

Raman spectra of calcined $LaCo_{1-x}Fe_xO_3$ were recorded using an optical neutral density filter to minimize the power of the excitation beam and prevent sample damage. Increasing the laser power

Fig. 3. Arrhenius plots ln k vs. 1/T for the decomposition of N_2O restricted to conversion in the range 5–15% during the temperature-programmed reaction with 0.1 vol% N_2O, 5 vol% NO, 6 vol% O_2 and 15 vol% H_2O on calcined (A) and aged (B) $LaCo_{1-x}Fe_xO_3$ catalysts.

at the sample from 0.2 to 0.8 mW produced a significant sample modification featuring the rapid emergence of strong fluorescence processes. As shown in Fig. 5A, the Raman spectrum of $LaFeO_3$ (f) is quite similar to previous observations [25] and characterizes a distorted orthorhombic perovskite structure with 24 Raman active modes. On the other hand, the Raman spectrum of $LaCoO_3$ (a) consists of two intensive bands respectively at 148 and 400 cm^{-1} previously assigned to E_g modes of rhombohedral perovskite [26]. However, we cannot completely rule out the presence of La_2O_3 characterized by a Raman active mode at 400 cm^{-1} [27]. Partially substituted $LaCo_{1-x}Fe_xO_3$ solids are quite different from $LaCoO_3$ and $LaFeO_3$. Two Raman signals appear at 561 and 694 cm^{-1} which intensify and shift to lower wavenumber values with an increase in Fe content. These bands cannot be attributed to any allotropic form of Fe_2O_3 nor to Fe_3O_4. Rousseau et al. [28] found almost the same Raman spectrum on $LaCo_{0.8}Fe_{0.2}O_3$ and they roughly assigned the main band (~694 cm^{-1}) to the A_{2g} breathing mode derived from the R-3c space group of rhombohedral perovksite. However, this suggestion seems controversial compared to XRD observations obtained on a series of solid solutions $LaCo_{1-x}Fe_xO_3$. More significant seems to be the strong correlation established between B—O bond length, estimated from XRD refinement (see Table 3), and the wavenumber of the most prominent Raman line, as illustrated in Fig. 5B. An attempt was done to fit that correlation with a linear regression. The Raman shift keeps linear up to $LaFeO_3$, which allows us to correlate this main band to the B—O line. In fact, B-site cations are present as centre of octahedral BO_6 building blocks in perovskite-type oxides (ABO_3). Therefore, the substitution of cobalt by iron in the B-site would result in a lengthening of B—O bond, consequently drive the Raman lines towards lower wavenumber. Although tentative, this assignment supported by XRD and rational structural considerations appears reasonable to explain the Raman features in $LaCo_{1-x}Fe_xO_3$ solid solutions. One have to mention that Raman spectral features on perovskite based materials are relatively scarce due to strong fluorescence phenomena. To our knowledge, this interesting correlation is firstly reported.

3.2.3. Tof-SIMS analysis

Secondary ion mass spectrometry (SIMS) can provide unique information on the coordination of one element with others by the emission of molecular clusters. In this study, hundreds of cluster ions were collected on calcined $LaCo_{1-x}Fe_xO_3$ solids. Special attention was paid to the evolution of $La_3Co_2O_6^+$, $La_3CoFeO_6^+$, $La_3Fe_2O_6^+$ clusters as a function of iron content in the perovskite. As summarized in Table S3, only $La_3Co_2O_6^+$ cluster was detected and analyzed on $LaCoO_3$. Iron insertion leads to the substitution of cobalt in the $La_3Co_2O_6^+$ and develops the consequent $La_3CoFeO_6^+$ and $La_3Fe_2O_6^+$ clusters on mixed $LaCo_{1-x}Fe_xO_3$ solids. This observation directly confirms a preferential formation of solid solutions at the topmost surface with cobalt and iron atoms coexisting in the B-site of perovskite. Due to the same chemical environment of cobalt and iron elements, a semi-quantitative surface analysis can be achieved from the intensity of selected clusters ions (Table S3). Relative cobalt content calculated from Co$^+$ and Fe$^+$ clusters
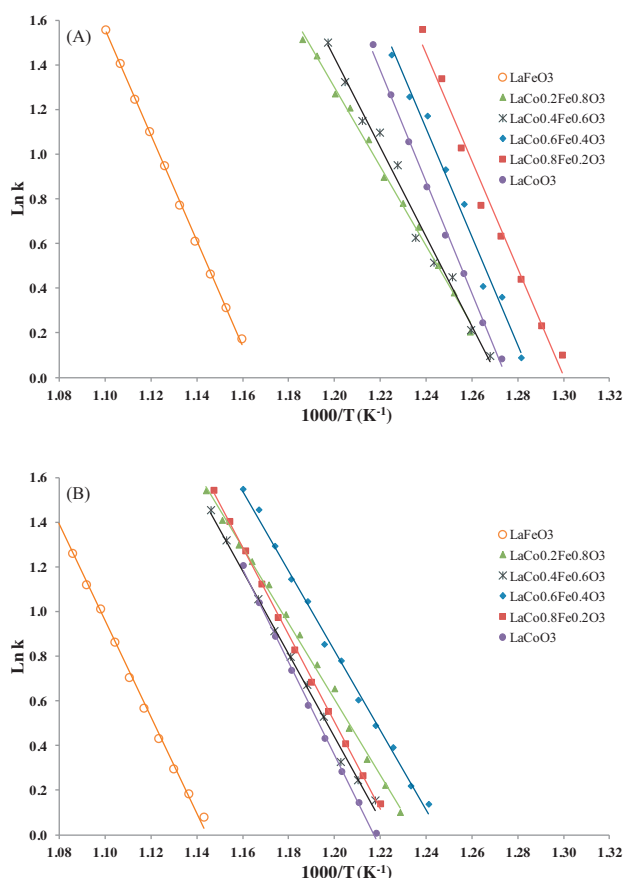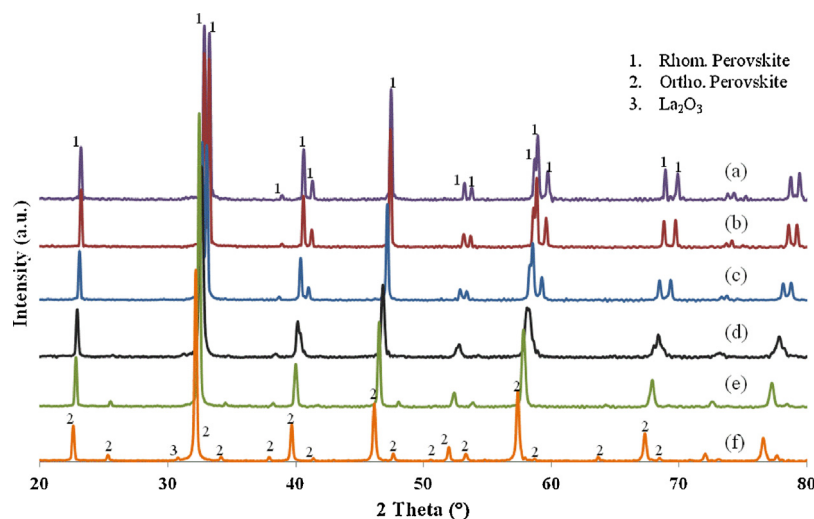
Fig. 4. XRD patterns of $LaCo_{1-x}Fe_xO_3$ solids calcined at 900 °C (a) $x=0$, (b) $x=0.2$, (c) $x=0.4$, (d) $x=0.6$, (e) $x=0.8$, (f) $x=1$.

is in good agreement with the theoretical one taking the margin of error into account. Similar results can also be obtained from $La_3Co_2O_6^+$, $La_3CoFeO_6^+$ and $La_3Fe_2O_6^+$ clusters. However, slightly larger deviation was found on $LaCo_{0.6}Fe_{0.4}O_3$ and $LaCo_{0.4}Fe_{0.6}O_3$, with calculated values of 0.50 and 0.32 respectively. This is perhaps due to a more complicate splitting of large clusters. The depth profiles of secondary Fe^+ and Co^+ ions were recorded on calcined $LaCo_{0.2}Fe_{0.8}O_3$ (Fig. 6). As illustrated by the relative intensity

$Fe^+/(Co^+ + Fe^+)$, slightly lower iron concentration is observed on the outer layer of solid and after several seconds' sputtering (>60 s), the relative intensity kept stable around its theoretical Fe content of 0.8, underlining an almost homogeneous distribution of cobalt and iron atoms in the bulk of perovskite.

3.2.4. X-ray photoelectron spectroscopy analysis

Analyzing the sample containing iron and cobalt species by XPS sometimes may be problematic, because the contributions of Fe and Co Auger peaks superimpose the characteristic Co 2p and Fe 2p photopeaks. This disruption is more pronounced on Fe 2p photopeaks. In this study, Fe and Co Auger peaks were recorded, respectively in Fig. 7B(f) and C(a), for further deconvolution of Co 2p and Fe 2p photopeaks.

Let us focus on the photopeaks of La 3d (Fig. 7A). The main peak at ∼883.7 eV on calcined $LaCo_{1-x}Fe_xO_3$ solids generally characterizes La^{3+} in the perovskite structure [29]. An additional contribution at 834.7 eV on $LaCoO_3$ is assigned to La_2O_3 as reported elsewhere [30]. This assignment seems in good agreement with Raman observations as aforementioned. The profiles of Co 2p photopeak reveal typically the Co^{3+} spectral features with a shake-up structure at ∼790 eV. However, Fe Auger peak prevents further analysis of Co^{2+} species by checking the satellite peak at ∼787 eV especially on $LaCo_{0.2}Fe_{0.8}O_3$. A slight shift of Co 2p photopeak towards lower binding energy was observed at high
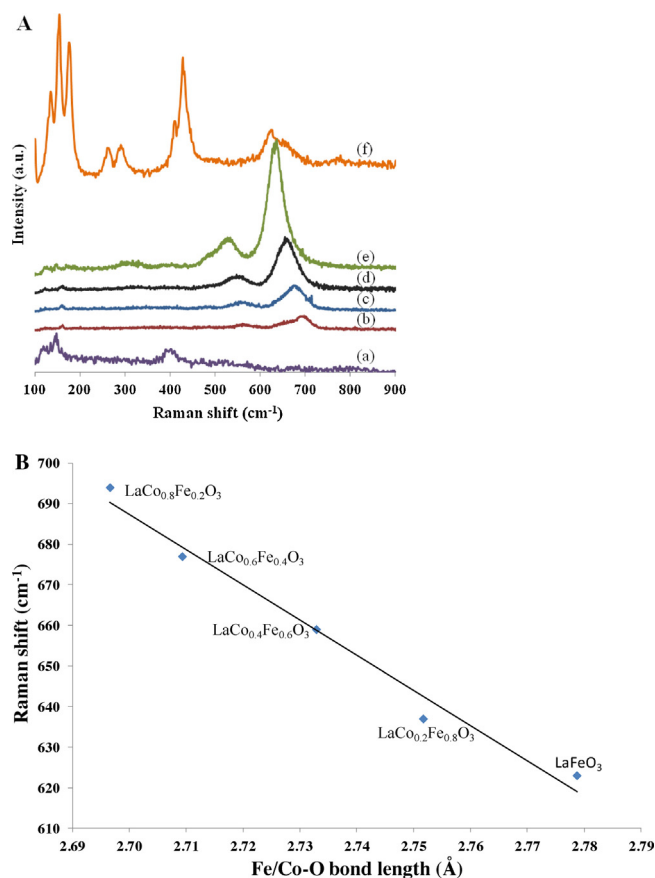

Fig. 5. Raman spectra recorded on $LaCo_{1-x}Fe_xO_3$ solids calcined at 900 °C (a) $x=0$, (b) $x=0.2$, (c) $x=0.4$, (d) $x=0.6$, (e) $x=0.8$, (f) $x=1$ (A). Raman shift of the main line as a function of Fe/Co—O bond length (B).
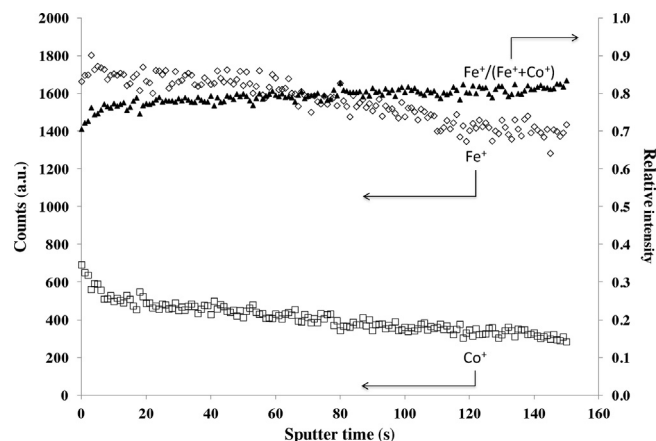

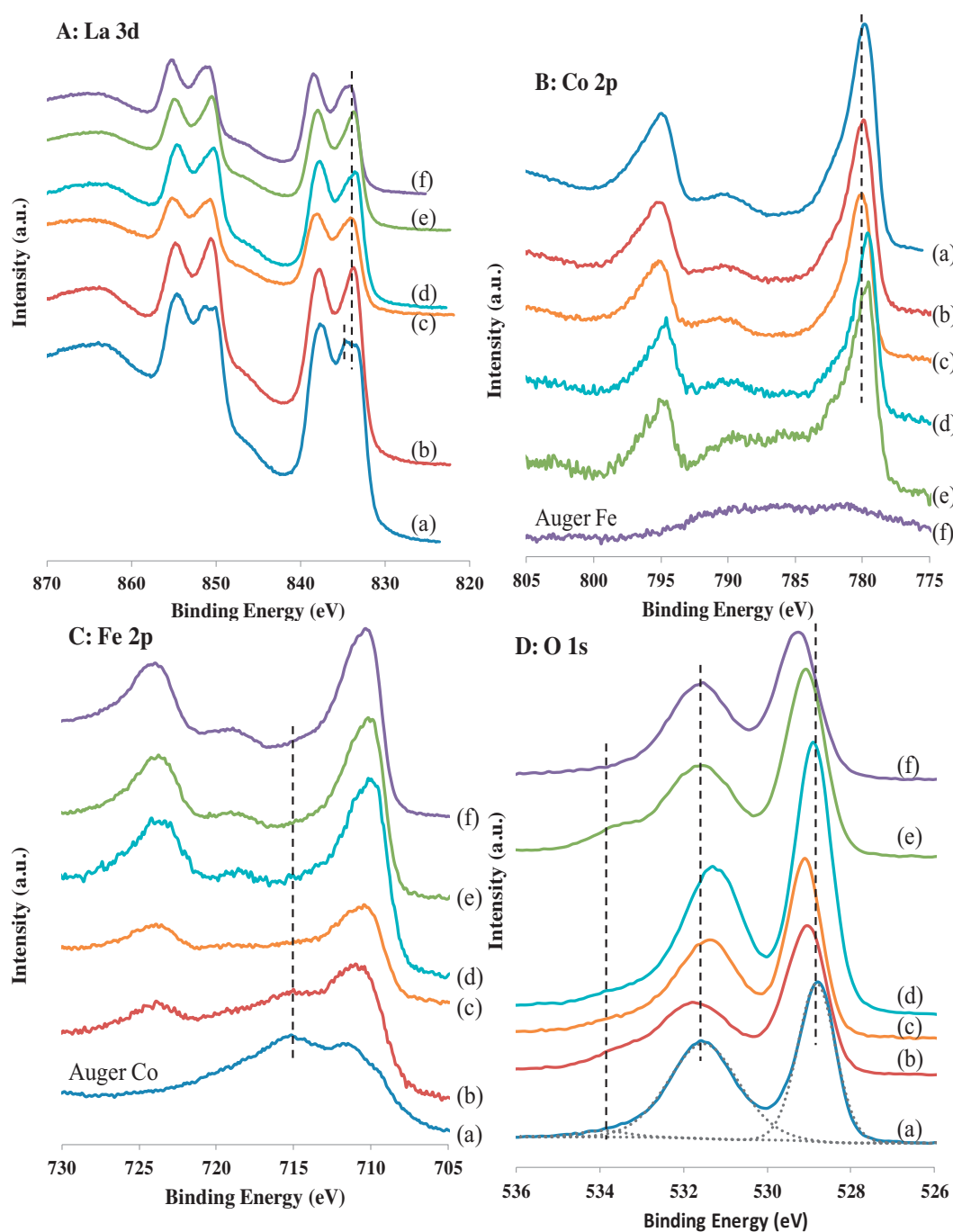**Fig. 6.** Tof-SIMS depth profiles of secondary ions Fe^+ and Co^+ on calcined $LaCo_{0.2}Fe_{0.8}O_3$.

Fig. 7. XPS La 3d (A), Co 2p (B), Fe 2p (C) and O 1s (D) photopeaks recorded on LaCo$_{1-x}$Fe$_x$O$_3$ solids calcined at 900 °C (a) $x = 0$, (b) $x = 0.2$, (c) $x = 0.4$, (d) $x = 0.6$, (e) $x = 0.8$, (f) $x = 1$.

Table 4
XPS analysis of LaCo$_{1-x}$Fe$_x$O$_3$ solids calcined at 900 °C.

	Binding energy (eV)		Surface composition[a]				
	O$_{1s}$	Co$_{2p5/2}$	O/La	Co/La[b]	Fe/La[b]	(Co + Fe)/La	Co/(Co + Fe)
LaCoO$_3$	528.8	779.8	3.30	0.58	–	0.58	1
LaCo$_{0.8}$Fe$_{0.2}$O$_3$	529.1	779.9	3.51	0.56	0.11	0.66	0.84
LaCo$_{0.6}$Fe$_{0.4}$O$_3$	529.1	780.0	3.15	0.48	0.21	0.69	0.70
LaCo$_{0.4}$Fe$_{0.6}$O$_3$	528.9	779.6	3.04	0.26	0.27	0.53	0.49
LaCo$_{0.2}$Fe$_{0.8}$O$_3$	529.1	779.5	3.74	0.26	0.45	0.61	0.26
LaFeO$_3$	529.3	–	3.27	–	0.47	0.47	0

[a] Relative accuracy ~20%.
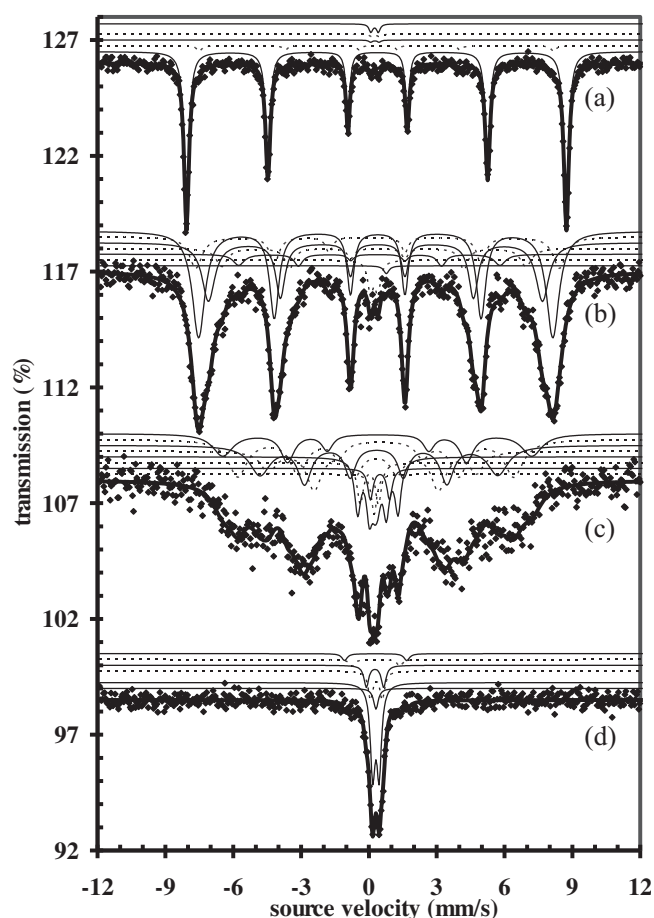[b] Surface composition estimated after subtraction of Fe and Co Auger contributions.

Fig. 8. Mössbauer spectra of calcined $LaCo_{1-x}Fe_xO_3$ solids (a) $x = 1$, (b) $x = 0.8$, (c) $x = 0.6$, (d) $x = 0.2$ recorded at room temperature.

iron content as summarized in Table 4. According to Dacquin et al. [31], this shift can be associated to the presence of Co^{2+} species after iron insertion in the perovskite. The Fe 2p photopeaks are more disturbed by Co Auger peak. But an average oxidation state of +3 can be concluded based on the binding energy of Fe $2p_{3/2}$ photopeak after subtraction of Co Auger contribution. Regarding the O1s photopeak in Fig. 7D, three types of oxygen are evidenced on calcined $LaCo_{1-x}Fe_xO_3$ solids. As reported elsewhere [32], the contribution between 528.8 and 529.3 eV can be ascribed to lattice oxygen O^{2-}, whereas the contribution at ~531.5 eV would correspond to adsorbed oxygen stabilized as CO_3^{2-}. OH groups and adsorbed molecular water are currently detected above 533.2 eV.

Table 4 summarizes the surface composition estimated after subtraction of Fe and Co Auger contributions. Surface La enrichment was found on calcined $LaCo_{1-x}Fe_xO_3$ solids as reported everywhere [33]. The Co/La and Fe/La atomic ratios vary according to their bulk composition. Compared to $LaFeO_3$, Co-containing samples show relatively higher (Co + Fe) surface concentration. The Co/(Co + Fe) surface atomic ratios are slightly higher than theoretical values. This deviation seems in good agreement with the depth profiles of elements obtained from Tof–SIMS analysis.

3.2.5. Mössbauer spectroscopy

As presented in Fig. 8, Mössbauer spectra of calcined $LaCo_{1-x}Fe_xO_3$ solids recorded at room temperature reveal a progressive modification of magnetic properties as a function of the iron composition x ($x = 1$, 0.8, 0.6 or 0.2). The hyperfine parameters and the quantification of each iron species are summarized in Table

S4. The assignment of iron species refers to previous investigations [34,35].

The $LaFeO_3$ spectrum (Fig. 8(a)) shows the sextet characteristic of $LaFeO_3$ phase (HF = 52.3 T) [36] and three small contributions which might be associated with residual iron oxides such as Fe_3O_4, $\gamma-FeOOH$ or $Fe_{1-y}O$. These iron oxides were not detected by other techniques due to their low amounts; however, segregated La_2O_3 phase evidenced by XRD on $LaFeO_3$ might imply the presence of iron oxides. In $LaFeO_3$ phase, the sextet corresponds to Fe^{3+} ions in the octahedron's center surrounded by six O^{2-} ions on (0 0 1), (1 0 0) and (0 1 0) faces whereas La^{3+} ions occupy eight corners of the orthorhombic unit cell ($a \approx b < c$ and $\alpha = \beta = \gamma = 90°$).Compared to $LaFeO_3$, a broadening of external lines of the spectrum is clearly evidenced on $LaCo_{0.2}Fe_{0.8}O_3$ as illustrated in Fig. 8(b). This indicates the presence of Fe^{3+} ions with different surroundings. It originates from cobalt and iron random distribution over six nearest neighbor sites of an iron ion. As increasing Co^{3+} ions in the neighborhood of the Fe^{3+} ion, the hyperfine field decreases. Thus, the sites characterized by a hyperfine field of 50.1, 48.8 and 46 T could be related to Fe^{3+} ions in the octahedral sites with respectively 0, 1 and 2 Co^{3+} ions in its neighborhood. The experimental abundances deviate from more or less the theoretical values calculated according to the binomial distribution proposed by Russo et al. [37]. However, when considering the slight distortion of the octahedron caused by a longer c-axis, our results seem reasonable. More intense distortion might take place when three cobalt ions occupy the neighbor sites of an iron ion. The distortion leads to not only the formation of tetrahedral sites but also higher oxidation state $Fe^{(3+\delta)+}$ species according to previous assignments [34,35]. An additional contribution with remarkably different isomer shift (IS = 0.036 mm/s) was also introduced to the spectrum fitting. This component has been attributed to Fe^{4+} ions and is consistent with previous findings [33,38]. As earlier discussed from XPS data, Co^{2+} species might exist at high iron content. Therefore, the presence of Fe^{4+} ions can compensate the electronic disturbances caused by the reduction of Co^{3+} in the sample.

Further substitution of iron by cobalt leads to the transition from a magnetically ordered state to a spin-disordered state as illustrates in Fig. 8(c). Similar deconvolution can be achieved on $LaCo_{0.4}Fe_{0.6}O_3$. The hyperfine fields of 42.6, 38, 32.8 and 5.6 T were attributed to Fe^{3+} ions in the octahedral sites with different Co^{3+} ion surroundings. Others are located either in distorted octahedral sites or tetrahedral sites if the distortion is more intense. $Fe^{(3+\delta)+}$ and Fe^{4+} species were also evidenced.

3.3. Bulk and surface characterization of aged $LaCo_{1-x}Fe_xO_3$

The catalysts after reaction were characterized by N_2 physisorption, XRD, XPS and Mössbauer spectroscopy. A decrease in specific surface area associated with an increase in crystallite size takes place on all the catalysts after reaction with 0.5 vol% NO. Exposure to higher NO concentration does not induce further changes in SSA and crystallite size which slightly vary (Table 5). XRD patterns recorded on the catalysts after ageing reveal the same phase with those already depicted on calcined samples with no detectable segregation of single metallic oxides. The cell parameters obtained from Rietveld refinement remain constant, underlining a general structural stability of perovskite-based materials under realistic conditions which highlights relative good thermal stability under wet atmosphere in the presence of 15 vol% H_2O.

XPS and Mössbauer spectroscopy provide complementary information on the surface properties in particular the evolution of oxidation state of cobalt and iron species after the reaction. As previously discussed, unusual oxidation state Fe^{4+} can exist on calcined $LaCo_{1-x}Fe_xO_3$ at high iron content. Table S5 summarizes the different iron species coexisting in the catalysts after reaction

with 0.5 vol% and 5 vol% NO. Based on these results, a successive degradation of Fe^{4+} to Fe^{3+} via $Fe^{(3+\delta)+}$ under reaction mixture is highlighted. Fig. 9 exemplifies XPS spectra recorded on the catalysts $LaCo_{1-x}Fe_xO_3$ after reaction in the presence of 0.5 vol.% and 5 vol.% NO and further compared with spectra earlier discussed on calcined samples. Particular attention was paid to the characteristic Co 2p, La 3d and Fe 2p photopeaks. Fig. 9A on $LaCoO_3$ emphasizes

previous observations related to the appearance of the higher B.E. contribution on the La 3d5/2 core level at 835.5 eV which intensifies after reaction especially in the presence of 5 vol% NO. This observation reflects the preferential formation of $La(OH)_3$ as reported elsewhere [30]. On the other hand, the predominant contribution at 883.7 eV characterizing La^{3+} species stabilized inside the perovskite structure is preserved showing the greatest stability of
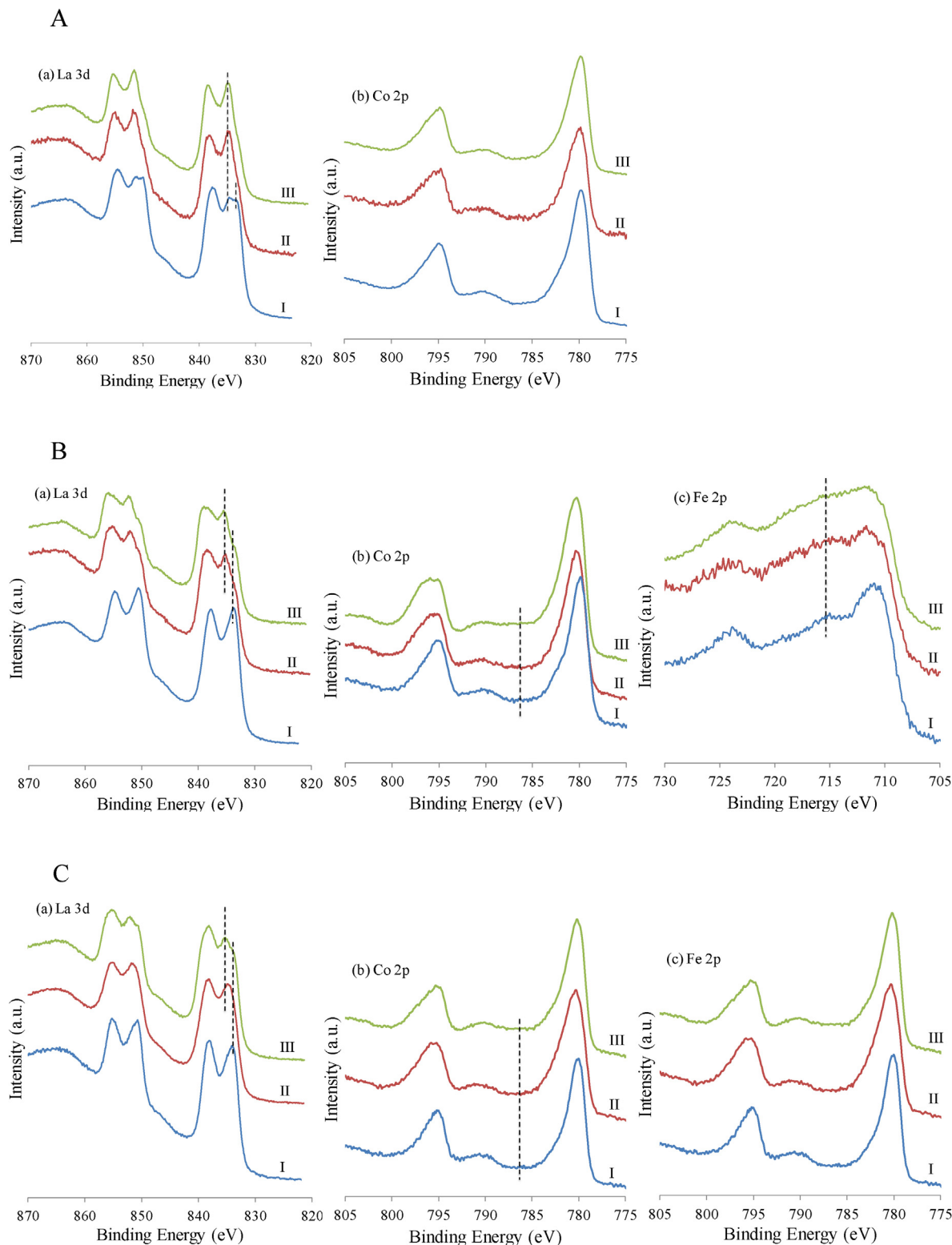

Fig. 9. XPS spectra of $LaCo_{1-x}Fe_xO_3$ catalysts (A) $x = 0$, (B) $x = 0.2$, (C) $x = 0.4$, (D) $x = 0.6$, (E) $x = 0.8$, (F) $x = 1$. Photopeaks of La 3d (a), Co 2p (b), Fe 2p (c) at different steps: (I) calcined catalysts, (II) after reaction with 0.5 vol% NO, (III) after reaction with 5 vol% NO.
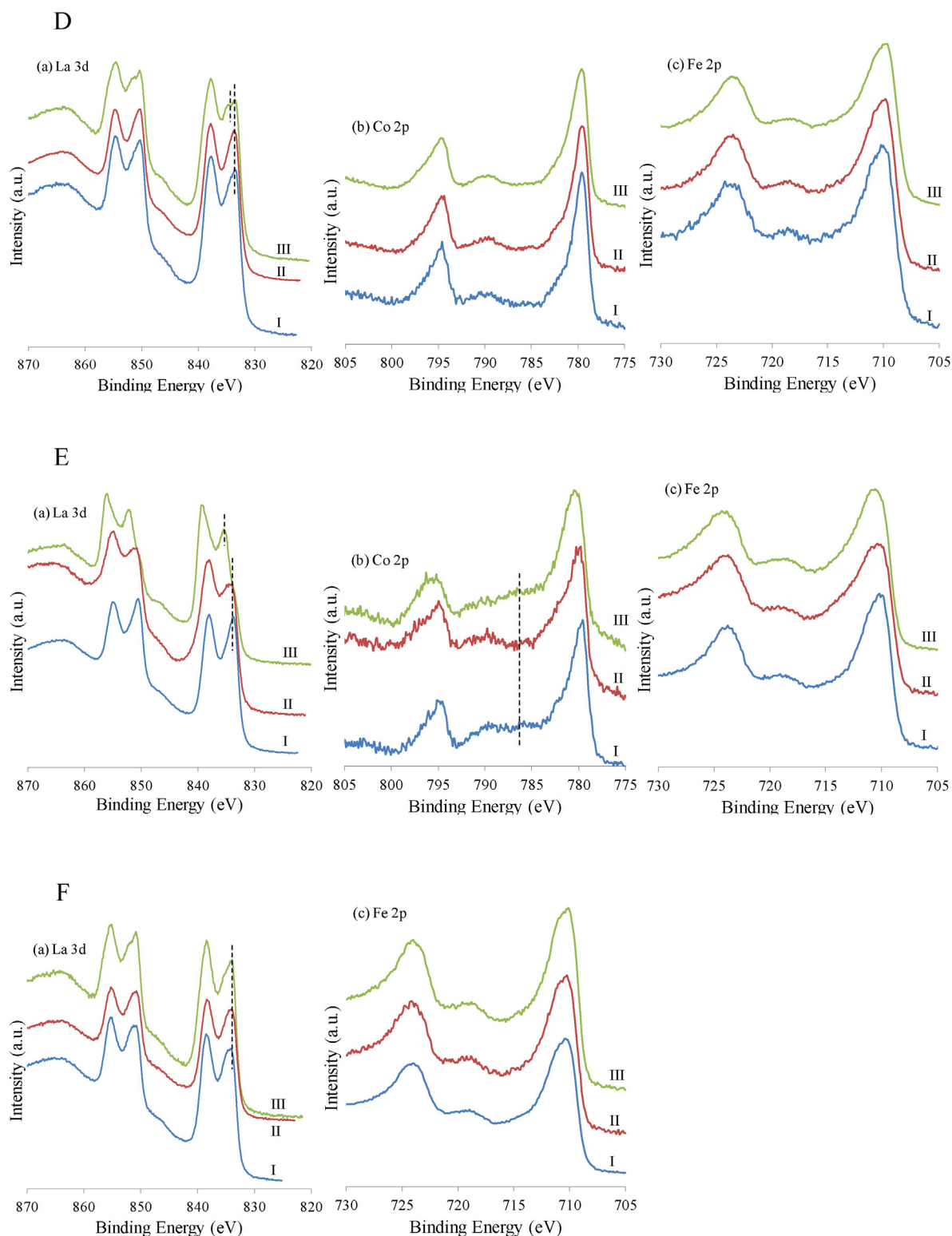
Fig. 9. (continued).

LaFeO$_3$ species avoiding significant surface segregation (Fig. 9F). Now regarding the Co 2p core level on LaCo$_{1-x}$Fe$_x$O$_3$, no significant change is discernible on calcined and aged samples submitted to 0.5 vol% NO. On the other hand, significant perturbations take place when samples are submitted to higher NO concentration related to a significant increase of the shakeup structure at 787 eV characterizing the presence of Co^{2+}. This trend seems more visible for

$x = 0.8$ which suggests for this composition a preferential surface segregation of La(OH)$_3$ and Co$_3$O$_4$ phases. Such partial extraction of cobalt has been already mentioned on Pd modified-LaCoO$_3$ catalyst after calcination at 800 °C [39]. Parallel to those observations the N 1s core level has been analyzed showing the development of two predominant contributions at 404 and 407 eV ascribed to nitrogen stabilized as nitrites and nitrates respectively. It seems obvious that

Table 5
Specific surface area and crystallite size of $LaCo_{1-x}Fe_xO_3$ catalysts after ageing at 900 °C in the presence of 0.5 vol% and 5 vol% NO.

	SSA (m^2/g)			Crystallite size[a] (nm)		
	Calcined	5 vol% NO	0.5 vol% NO	Calcined	0.5 vol% NO	5 vol% NO
$LaCoO_3$	4.6	2.9	2.8	75	102	108
$LaCo_{0.8}Fe_{0.2}O_3$	4.5	2.4	2.7	67	84	55
$LaCo_{0.6}Fe_{0.4}O_3$	5.4	3.0	2.6	53	70	68
$LaCo_{0.4}Fe_{0.6}O_3$	5.6	3.9	2.9	31	34	34
$LaCo_{0.2}Fe_{0.8}O_3$	4.6	2.9	3.1	48	57	58
$LaFeO_3$	4.4	2.5	2.2	34	69	62

[a] Crystallite size was estimated by Rietveld refinement.

Table 6
XPS analysis of $LaCo_{1-x}Fe_xO_3$ catalysts after ageing at 900 °C with 0.5% and 5% NO.

	Calcined[a]			Reaction with 0.5% NO[a]				Reaction with 5% NO[a]			
	O/La	Co/La	Fe/La	O/La	Co/La	Fe/La	N/La	O/La	Co/La	Fe/La	N/La
$LaCoO_3$	3.30	0.58	–	4.72	0.67	–	0.59	4.35	0.61	–	0.43
$LaCo_{0.8}Fe_{0.2}O_3$	3.51	0.56	0.11	4.99	0.63	0.09	0.77	6.08	0.81	0.13	0.97
$LaCo_{0.6}Fe_{0.4}O_3$	3.15	0.48	0.21	3.21	0.36	0.19	0.08	4.91	0.47	0.24	0.57
$LaCo_{0.4}Fe_{0.6}O_3$	3.04	0.26	0.27	3.12	0.27	0.31	0.18	4.17	0.33	0.38	0.42
$LaCo_{0.2}Fe_{0.8}O_3$	3.74	0.26	0.45	3.94	0.13	0.39	0.13	6.58	0.15	0.43	1.40
$LaFeO_3$	3.27	–	0.47	3.09	–	0.44	0.12	3.87	–	0.57	0.45

Atomic Co/La and Fe/La estimated after subtraction of Fe and Co Auger contributions.

[a] Relative accuracy ~20%.

a greater stabilization, reflected by the quantification of the atomic N/La ratio (see Table 6), takes place on $LaCo_{0.2}Fe_{0.8}O_3$ correlatively to the segregation of the single La and Co oxides suggested by the examination of the La 3d and Co 2p photopeaks.

4. Discussion

The purpose of this study was focused on the impact of NO concentration on the catalytic behavior in terms of activity and stability of $LaCo_{1-x}Fe_xO_3$ perovskites in the decomposition of N_2O at moderate and high temperature. Particular attention was paid to the impact of thermal ageing overnight in reactive conditions at 900 °C on the catalytic properties. Realistic conditions were selected for lab-scale measurements in the presence of 15 vol% H_2O and 5 vol% NO contrarily to most of previous investigations which usually report experimental data generally obtained in mild conditions which are not easily transferable for further practical developments [7,40,41]. According to these realistic experimental conditions, it was found that different reversible/irreversible deactivation processes taking place at moderate or high temperature, of respectively 525 and 900 °C, can alter the properties of calcined and aged $LaCo_{1-x}Fe_xO_3$ catalysts as summarized in Fig. 10 based on the calculation of specific and intrinsic rates. Rough rate calculation accounts for Tof-SIMS and XPS measurements which do not evidence significant deviation between bulk and surface Co and Fe compositions and taking into account the negligible activity of $LaFeO_3$ at 525 °C. Subsequent correlation with the B—O bond length can be established on calcined catalysts. On the other hand such correlation disappears on aged samples irrespective of iron content. By examining literature data, it is sometimes ambiguous to explain the catalytic properties of perovskite based materials taking a wide panel of structural and electronic factors into account. For instance, the coordination of transition metals may induce changes in the catalytic properties with longer B—O bond originating weaker bond strength as seen in Fig. 10 on calcined $LaCo_{1-x}Fe_xO_3$. However, sometimes no correlation can be established especially on $La_{2-x}Sr_xCuO_{4-y}$ structure when oxygen is co-fed with N_2O [42]. Hence, aged $LaCo_{1-x}Fe_xO_3$ samples would exhibit a comparable behavior as that previously observed on $La_{2-x}Sr_xCuO_{4-y}$. More recently, Kondratenko et al. [13,14] investigated the micro-kinetics

of direct N_2O decomposition on $BaFeAl_{11}O_9$ and Fe-MFI zeolites from TAP measurements. They found that the degree of clustering of FeO_x species affects the kinetic parameters influencing the collision frequency of N_2O with reactive oxygen species and also the activation energy.

4.1. Catalytic behavior of calcined $LaCo_{1-x}Fe_xO_3$ vs. bulk and surface properties

As reported elsewhere, N_2O decomposition is usually recognized to be sensitive to oxygen mobility. By way of illustration, Ivanov et al. [43] observed that the increased rate values on $La_{1-x}Sr_xMnO_3$ compared to $LaMnO_3$ are related to a faster pathway for oxygen transfer through the creation of oxygen vacancies in the perovskite lattice to compensate the reduced cation charge. Nitadori and Misono [44] proposed that the oxygen desorption is always accompanied with the reduction of B-site elements. Electronic properties of $LaCo_{1-x}Fe_xO_3$ were investigated by XPS and Mössbauer spectroscopy. They underline the oxidation state of +3 for most of cobalt and iron species in calcined catalysts. At high iron content, the binding energy of Co $2p_{3/2}$ slightly shifts
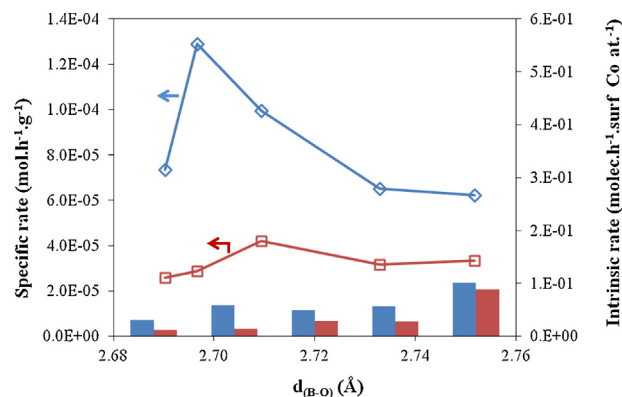
Fig. 10. Correlation between specific and intrinsic rate constants calculated at 525 °C on calcined (blue) and aged $LaCo_{1-x}Fe_xO_3$ catalysts (red) vs. the B—O bond length with B=Co or Fe. (For interpretation of the references to color in this figure legend, the reader is referred to the web version of the article).

to lower values, indicating the presence of Co^{2+}. The electronic disturbance caused by the reduction of Co^{3+} is likely compensated by the unusual high oxidation state of iron as Fe^{4+} in agreement with Mössbauer spectroscopic observations. However, such observations seem in good agreement with previous ones reported by Nitadori and Misono [44] showing that an increase in Co^{2+} would likely compensate the creation of anionic vacancied promoted by faster oxygen desorption on $LaCo_{0.2}Fe_{0.8}O_3$.

Returning to bulk characterization of calcined $LaCo_{1-x}Fe_xO_3$, the examination of XRD patterns reveals a continuous modification from rhombohedral structure for $x = 0$ ($LaCoO_3$) towards orthorhombic structure for $x = 1$ ($LaFeO_3$). Iron insertion in the framework of $LaCoO_3$ leads to an expansion of the unit cell volume and a subsequent weakening of the B—O bond as shown in Table 3. Raman spectroscopy also provides original results with spectral features correlated to structural parameters emphasizing the formation of solid solutions. Hence, further comparison between intrinsic rate expressed per surface Co atom calculated at 525 °C shows a good correlation with the Co—O distance showing a rate enhancement with longer Co—O bond and emphasizing the hypothesis that the oxygen mobility and related reactivity of those mobile oxygen species would govern the catalytic properties. Significant lessening of the apparent activation energies after iron substitution especially on $LaCo_{0.2}Fe_{0.8}O_3$ would reflect faster oxygen desorption with related formation of anionic vacancies.

4.2. Impact of NO concentration and thermal ageing on the catalytic behavior of calcined $LaCo_{1-x}Fe_xO_3$: correlation with bulk and surface properties

At low temperature ($T = 525$ °C), the presence of NO, H_2O and oxygen must be taken into account because they compete for adsorption both on calcined and aged catalysts and could likely originate new reaction pathways for N_2O decomposition and/or changes in the relative rates of elementary steps involved in N_2O decomposition as reported elsewhere [13,14]. As exemplified, NO should play a specific role associated with the production of NO_2 accelerated on Co-riched samples. It is interesting to note that Temperature-Programmed Reaction experiments on $LaCoO_3$ reveal a rate enhancement above the light-off temperature with a rise in NO concentration (Fig. S1). Previous investigations highlight the beneficial effect of NO enhancing oxygen desorption commonly recognized as rate determining step and lowering the apparent activation energy of N_2O decomposition [45]. Such observation has also been reported by Smeets et al. [46] who suggested that the acceleration of oxygen recombination provides an alternative route for oxygen migration via gas-phase NO_2 on Cu/zeolite based catalysts. Again, they observed a significant decrease of the apparent activation energy especially at low Cu loading. Differences also arose in the pre-exponential factor as a function of Cu loading explained by the dependence on the distance between two Cu—O centers to accelerate the recombination of atomic oxygen species. All these trends agree with our observations on the apparent activation energies and pre-exponential values reported in Tables 1 and 2 especially on $LaCo_{0.2}Fe_{0.8}O_3$ with low pre-exponential value likely related to lower probability for finding two Co—O center at an appropriate distance and in parallel low apparent activation energy pointing out a compensating effect usually observed irrespective of the NO partial pressure and the degree of deactivation. Again, the effect of Fe increasing the mobility of surface oxygen species is underlined. Further stabilization of nitrates species evidenced on all the catalysts may strongly inhibits the rate of N_2O decomposition at low temperature. This would correctly explain the lower values for the pre-exponential factors estimated in the presence of 5 vol% NO compared with those calculated with 0.5 vol% NO. It is ascribed to higher ad-NO_x coverage with an increasing NO partial

pressure as pointed out by the comparison of the atomic N/La ratio values in Table 6. The beneficial effect of NO capable to restore active sites through the removal of hydroxyl groups at the catalyst surface [45,47] seems also in contradiction with XPS observations since the examination of the La 3d core level clearly underlines the growth of $La(OH)_3$ with an increase in NO concentration (see Fig. 9).

Now, by comparing both the specific and intrinsic rates (see Fig. 10), it seems obvious that thermal ageing induces deactivation on all the catalysts. As previously discussed such deactivation is not related to loss of structural properties relatively stable in these severe operating conditions. At the same time the weak loss of specific surface area cannot be responsible of the loss of activity in N_2O conversion. Surface characterization by XPS and Mössbauer spectroscopy provides evidences which can partly explain deactivation phenomena revealing that high temperature in conjunction with high NO concentration probably originate such deactivation. In a first approach, the detection of Fe^{4+} on calcined catalysts can be considered as a probe to roughly examine changes in the oxygen mobility. As found, the disappearance of Fe^{4+} on aged samples would suggest that oxygen mobility is altered. However, at the same time, the proportion of Co^{2+} increases on all the catalysts but more significantly on $LaCo_{0.2}Fe_{0.8}O_3$ especially when thermal ageing is performed in the presence of 5 vol% NO. Such formation would be more related to Co extraction from the perovkite structure to form Co_3O_4 segregating at the surface in accordance with similar trends reported elsewhere [48]. While it has been demonstrated that Co_3O_4 is intrinsically active in N_2O decomposition [49,50] a greater stabilization of nitrate species could explain the lowest activity at 525 °C recorded on aged samples. Finally, the impact of Co extraction from the perovskite lattice and subsequent CoO_x clustering can also be rationalized on the basis of previous findings reported elsewhere [13]. Kondratenko et al. compared the activity of $BaFeAl_{11}O_{19}$ and Fe-MFI in N_2O decomposition and observed differences due to the degree of clustering of FeO_x species. This influences the collision frequency of N_2O with reactive oxygen species and also activation energy values which decrease substantially. Direct comparison with our results would not be obvious due to the pressure gap and the occurrence of competitive adsorption/reaction in the presence of large amount of NO_x which form ultimately stable ad-NO_x species and can alter both the pre-exponential factor and the apparent activation energy values as previously discussed. However, it is worthwhile to note that those authors observed after subsequent calcination and steam treatment at 600 °C a complete extraction of isomorphously substituted iron and subsequent clustering of extraframework highly dispersed iron oxide species which would originate changes observed on the kinetic parameters. Returning to our observations, a slight increase of the pre-exponential value is discernible at high Fe content (see Table 1) typically for $x \geq 0.6$ which could be in connection with explanations given by Kondratenko et al. [13]. As a matter of fact, previous interpretations in connection with the optimal distance between two Co centers to accelerate oxygen recombination [46] does not seem in contradiction with the explanation given by Kondratenko et al. who suggested that the rate of N_2O decomposition is controlled by the rearrangement of bi-atomic oxygen intermediate before desorption.

5. Conclusion

This investigation was focused on the high temperature N_2O decomposition on perovskite-based materials. Particular attention was paid on the impact of NO concentration close to the real composition of the exhaust gas coming from ammonia burner in nitric acid plants. This solution can be cost effective because of the thermal stability of the solids investigated with improved structural properties of $LaCoO_3$ due to iron insertion and their remarkable

selectivity. Indeed, no NO loss was observed especially at high NO concentration which might favor its decomposition. XRD and Raman spectroscopy highlighted the formation of solid solutions preserved after ageing in the presence of 0.1 vol% N_2O, 5 vol% NO, 6 vol% O_2 and 15 vol% H_2O. Catalytic properties have been quantified at moderate temperature (525 °C) on the basis of calculated kinetic parameters which showed the best compromise between intrinsic activity and stability for $LaCo_{0.2}Fe_{0.8}O_3$ with catalytic performances correlated to the length of the Co—O bond. On the other hand, this correlation disappear after ageing at 900 °C especially in the presence of 5 vol% NO. Surface segregation of Co_3O_4 would take place strengthening the formation of nitrates and then inhibiting the decomposition of N_2O.

Acknowledgements

Appendix A. Supplementary data

Supplementary data associated with this article can be found, in the online version, at http://dx.doi.org/10.1016/j.apcatb.2013.04.002.

References

[1] F. Kapteijn, J.A. Rodriguez-Mirasol, J.A. Moulijn, Applied Catalysis B 9 (1996) 25.
[2] J. Pérez-Ramírez, F. Kapteijn, G. Mul, X. Xu, J.A. Moulijn, Catalysis Today 76 (2002) 325.
[3] S. Alini, F. Basile, S. Blasioli, C. Rinaldi, A. Vaccari, Applied Catalysis B 70 (2007) 323.
[4] B. Coq, M. Mauvezin, G. Delahay, J.B. Butete, S. Kieger, Applied Catalysis B 27 (2000) 193.
[5] J. Pérez-Ramírez, F. Kapteijn, K. Schoffel, J.A. Moulijn, Applied Catalysis B 44 (2003) 117.
[6] P. Granger, P. Esteves, S. Kieger, L. Navascues, G. Leclercq, Applied Catalysis B 62 (2006) 236.
[7] F.J. Perez-Alonso, I. Melián-Cabrera, M. López-Granados, F. Kapteijn, J.L.G. Fierro, Journal of Catalysis 239 (2006) 340.
[8] P. Esteves, Y. Wu, C. Dujardin, M.K. Dongare, P. Granger, Catalysis Today 176 (2011) 433.
[9] G. Giecko, T. Borowiecki, W. Gac, J. Kruk, Catalysis Today 137 (2008) 403.
[10] J. Pérez-Ramírez, M. Santiago, Chemical Communications (6) (2007) 619.
[11] W. Burckardt, M. Voigt, EP 1147813 A2, 2001, to Porzellanwerk Kloster Veilsdor.
[12] J. Neumann, L. Isopova, L. Pinaeva, N. Kulikovskaya, L. Zolotarskii, WO2007104403 A1), 2007, to Umicore.
[13] E.V. Kondratenko, V.A. Kondratenko, M. Santiago, J. Pérez-Ramirez, Applied Catalysis 99 (2010) 66.
[14] E.V. Kondratenko, V.A. Kondratenko, M. Santiago, J.P. Ramirez, Journal of Catalysis 256 (2008) 248.
[15] M.A. Pena, J.L. Fierro, Chemical Reviews 101 (2001) 1981.
[16] J.P. Dacquin, C. Lancelot, C. Dujardin, P. Da Costa, G. Djega-Mariadassou, P. Beaunier, S. Kaliaguine, S. Vaudreuil, S. Royer, P. Granger, Applied Catalysis B 91 (2009) 596.
[17] I. Twagirashema, M. Engelmann-Pirez, M. Frere, L. Burylo, L. Gengembre, C. Dujardin, P. Granger, Catalysis Today 119 (2007) 100.
[18] J. Rodriguez-Carvajal, Physica B 192 (1993) 55.
[19] J. Rodríguez-Carvajal, in Commission on Powder Diffraction (IUCr) Newsletter 26 (2001) 12–19.
[20] D.A. Shirley, Physical Review B 5 (1972) 4709.
[21] Y. Wen, C. Zhang, H. He, Y. Yu, Y. Teraoka, Catalysis Today 126 (2007) 405.
[22] Y. Wu, X. Ni, A. Beaurain, C. Dujardin, P. Granger, Applied Catalysis B 125 (2012) 149.
[23] L. Bedel, A.C. Roger, C. Estournes, A. Kiennemann, Catalysis Today 85 (2003) 207.
[24] R.D. Shannon, Acta Crystallographica. Section A, Crystal Physics, Diffraction, Theoretical and General Crystallography 32 (1976) 751.
[25] M. Popa, J. Frantti, M. Kakihana, Solid State Ionics 154 (2002) 437.
[26] M. Popa, J. Frantti, M. Kakihana, Solid State Ionics 154 (2002) 135.
[27] L.M. Cornaglia, J. Múnera, S. Irusta, E.A. Lombardo, Applied Catalysis A 263 (2004) 91.
[28] S. Rousseau, S. Loridant, P. Delichere, A. Boreave, J.P. Deloume, P. Vernoux, Applied Catalysis B 88 (2009) 438.
[29] H. Taguchi, S. Yamada, M. Nagao, Y. Ichikawa, K. Tabata, Materials Research Bulletin 37 (2002) 69.
[30] M.F. Sunding, K. Hadidi, S. Diplas, O.M. Løvvik, T.E. Norby, A.E. Gunnæs, Journal of Electron Spectroscopy and Related Phenomena 184 (2011) 399.
[31] J.P. Dacquin, C. Dujardin, P. Granger, Journal of Catalysis 253 (2008) 37.
[32] S. Ponce, M.A. Pena, J.L.G. Fierro, Applied Catalysis B 24 (2000) 193.
[33] N.A. Merino, B.P. Barbero, P. Grange, L.E. Cadus, Journal of Catalysis 231 (2005) 232.
[34] I.D. Fawcett, G.M. Veith, M. Greenblatt, M. Croft, I. Nowik, Solid State Science 2 (2000) 821.
[35] P.S. Beurmann, V. Thangadurai, W. Weppner, Journal of Solid State Chemistry 174 (2003) 392.
[36] K. Swierczek, J. Marzec, D. Palubiak, W. Zajac, J. Molenda, Solid State Ionics 177 (2006) 1811.
[37] U. Russo, L. Nodari, M. Faticanti, V. Kuncser, G. Filoti, Solid State Ionics 176 (2005) 97.
[38] R.R. Kondakindi, A. Kundu, K. Karan, B.A. Peppley, A. Qi, C. Thurgood, P. Schurer, Applied Catalysis A 390 (2010) 271.
[39] G.L. Chiarello, J.D. Grunwald, D. Ferri, F. Krumeich, C. Oliva, L. Forni, A. Baiker, Journal of Catalysis 252 (2007) 127.
[40] J. Pérez-Ramírez, F. Kapteijn, J.C. Groen, A. Doménech, G. Mul, J.A. Moulijn, Journal of Catalysis 214 (2003) 33.
[41] A. Bueno-López, I. Such-Basáñez, C. Salinas-Martínez de Lecea, Journal of Catalysis 244 (2006) 102.
[42] J. Christopher, C.S. Swamy, Journal of Molecular Catalysis 62 (1990) 69.
[43] D.V. Ivanov, E.M. Sadovskaya, L.G. Pinaeva, L.A. Isupova, Journal of Catalysis 267 (2009) 5.
[44] T. Nitadori, M. Misono, Journal of Catalysis 93 (1985) 459.
[45] H. Xia, K. Sun, Z. Liu, Z. Feng, P. Ying, C. Li, Journal of Catalysis 270 (2010) 103.
[46] P.J. Smeets, B.F. Sels, R.M. van Teeffelen, H. Leeman, E.J.M. Hensen, Journal of Catalysis 256 (2008) 183.
[47] P.K. Roy, R. Prins, G.D. Pirngruber, Applied Catalysis B 80 (2008) 226.
[48] G.L. Chiarello, J.-D. Grunwaldt, D. Ferri, F. Krumeich, C. Oliva, L. Forni, A. Baiker, Journal of Catalysis 252 (2007) 127.
[49] G. Maniak, P. Stelmachowski, J.J. Stanek, A. Kotarba, Z. Sojka, Catalysis Communications 15 (2011) 127.
[50] P. Stelmachowski, F. Zasada, G. Maniak, P. Granger, M. Inger, M. Wilk, A. Kotarba, Z. Sojka, Catalysis Letters 130 (2009) 637.